JOURNAL OF GEOPHYSICAL RESEARCH, VOL. 102, NO. D5, PAGES 6081-6098, MARCH 20, 1997

An integrated air pollution modeling system for urban and regional scales: 2. Simulations for SCAQS 1987

Rong Lu and Richard P. Turco

Department of Atmospheric Sciences, University of California, Los Angeles

Mark Z. Jacobson

Department of Civil Engineering, Stanford University, Stanford, California

Abstract. A new air quality modeling system, the surface meteorology and ozone generation (SMOG) model, is used to investigate the evolution and properties of air pollution in the Los Angeles basin during the southern California air quality study (SCAQS) intensive field program. The SMOG model includes four major components: a meteorological model, a tracer transport code, a chemistry and aerosol microphysics model, and a radiative transfer code. The fidelity of the coupled modeling system is evaluated by comparing model predictions against SCAQS data. Predictions of surface winds and temperatures are found to be in excellent agreement with measurements during daylight hours, when a strong sea breeze and mountain-upslope flows are predominant but are less reliable at night when winds are typically lighter and more variable. Winds aloft, including shear and temporal variations, are also simulated quite well, although the forecasts (which are not constrained through continuous data assimilation) tend to drift from actual conditions as time progresses. Accordingly, the large-scale flow is reinitialized each morning in the simulations. The dispersion patterns of two inert tracers released during the SCAQS period are accurately reproduced by the model. The two releases, one in the early morning hours and one around noon, led to quite different transport rates and distributions owing to the evolution of the sea breeze over the course of the day. Overall, the three-dimensional development of thermally induced winds and their influences on tracer transport in the Los Angeles basin are accurately captured by the model. The predicted surface concentrations of ozone and other key pollutants have been spatially and temporally correlated with measured abundance, and the values agree to within 25-30% for ozone, with somewhat larger mean differences for several other species. In the case of the vertical distribution of ozone, the SMOG simulations generate dense oxidant (ozone) layers embedded in the temperature inversion, explaining for the first time similar features seen during SCAQS. Sources of error and uncertainty in the simulations are identified and discussed. The broad agreement between SMOG model predictions and SCAQS observations suggests that an integrated modeling approach is well suited for representing the coupled effects of mesoscale meteorology, tracer dispersion, and chemical transformations on urban and regional air quality.

1. Introduction

A comprehensive modeling system has been developed for air pollution studies on urban and regional scales (the surface meteorology and ozone generation (SMOG) model, which is described by *Lu et al.* [this issue], (hereinafter referred to as paper 1)). The SMOG model includes detailed treatments of mesoscale and boundary layer meteorology, tracer transport and dispersion, chemical and aerosol microphysical processes, and solar and terrestrial radiative transfer. This approach incorporates the entire set of basic atmospheric processes that are relevant to air pollution problems in a variety of urban airsheds. Hence an integrated model based on this approach could have wide applications. However, it is critical to test the individual algorithms that represent specific physical and chemical processes, to validate the accuracy of the major components of the model, and to determine the fidelity of simulations carried out under conditions where adequate observations are available to evaluate errors statistically. The basic algorithms and components have already been extensively tested in a series of works [*Jacobson*, 1994; *Jacobson and Turco*, 1994, 1995; *Jacobson et al.*, 1994, 1996a, b; *Lu*, 1994; *Lu and Turco*, 1994, 1995, 1996]. In the present study we therefore focus on the performance of the coupled modeling system.

For at least several decades, the Los Angeles basin in southern California has suffered from some of the most severe photochemical air pollution in the world. Photochemical smog in Los Angeles is associated with several factors including (1) large emissions of primary pollutants, mainly nitrogen oxides (NO_x) and nonmethane hydrocarbons (NMHC), that can generate ozone via photochemical processes; and (2) meteorological conditions suitable for the

Paper number 96JD03502.
0148-0227/97/96JD-03502$09.00

generation and accumulation of smog, principally the strong regional-scale temperature inversion, stagnant air, clear skies, and copious sunlight associated with a high-pressure system. The spatial distributions of pollutants over the Los Angeles basin are controlled to a large extent by thermally induced winds embedded in the large-scale airflow over complex local topography [*Lu and Turco*, 1994, 1995]. Moreover, meteorological dispersion and chemical transformation interact strongly in determining the abundances of trace species. Accordingly, a modeling system that accounts for all of these processes is needed to simulate the evolution of air pollution in a complex airshed. In this study the SMOG model is applied to the Los Angeles region for a specific period corresponding to the 1987 southern California air quality study (SCAQS). The model is used to predict a wide range of variables that can be compared to data collected in the field during SCAQS.

Several techniques are used to make quantitative and qualitative comparisons between model simulations and observations. Graphical comparisons of predicted fields (e.g., surface winds, ozone concentration maps, and vertical profiles) with measured fields can reveal the overall qualitative fidelity of the model. These comparisons demonstrate the ability to reproduce major structural features and behaviors. To obtain a more quantitative measure of model performance, we have adopted statistical procedures previously defined for this purpose [e.g., *Keyser and Anthes*, 1977; *Willmott et al.*, 1985; *Tesche et al.*, 1990]. The primary statistical measures used in this study include the standard deviations of the observed and calculated fields, the root-mean-square difference between the observed and predicted fields, and the "index of agreement," normalized gross error, and bias of the simulations in light of measurements.

In air quality modeling, errors can be introduced from a variety of sources, including parameters and data used in the numerous calculations, and approximations used in representing physical and chemical processes (not to mention possible numerical bugs in the codes; these latter errors have presumably been eliminated by rigorous algorithm testing). Specifically, errors may arise in the meteorological predictions of winds and boundary layer depths, in the emission rates of the primary pollutants contributing to smog formation, in the simulation of tracer transport, dispersion and deposition, and in the calculation of chemical and microphysical processing rates. Since the influence of trace pollutants on atmospheric dynamics is usually small, the meteorology predictions can be evaluated using observed meteorological data alone. Moreover, winds and turbulence determine the dispersion of inert tracers in the atmosphere, once the sources have been ascertained. Hence inert tracer data collected in controlled injection experiments can be used to verify the coupled meteorological predictions and tracer dispersion simulation. Chemically active tracers and aerosols, on the other hand, are affected by all of the model components. Verification of the distributions of these species must be carried out consistently with the validation of the meteorology and tracer dispersion. For many tracers, the largest uncertainties can be associated with inaccurate estimates of emission rates. In these instances, the validation process may actually lead to improved emission values. The most difficult variables to check are those for which there is little observational data, or inadequate emission data, or both. Accordingly, a carefully constructed phenomenology based on algorithms tested independently (for example, use of a detailed photochemical mechanism designed using smog chamber measurements) is the most reasonable approach to air quality simulation.

The structure of the SMOG model is described at length in paper 1 [*Lu et al.*, this issue] and related articles. In this paper the integrated modeling system is applied to analyze the substantial set of measurements obtained in the Los Angeles basin on August 27 and 28, 1987, during SCAQS. Section 2 lays out the SCAQS databases used for the model simulations and comparisons. Details of the particular simulations conducted for the SCAQS days, and comparisons with corresponding observations, are provided in section 3. Specifically, the model configuration and initialization for the simulations is summarized in section 3.1. In section 3.2, the meteorological predictions are assessed, and in section 3.3, the tracer dispersion experiments are analyzed in view of the calculated meteorological fields. The predicted and observed distributions of ozone and other key pollutants are assessed for spatial and temporal conformation in section 3.4. The sources of uncertainty in the model simulations are analyzed in section 3.5. Section 4 summarizes our major conclusions.

2. Southern California Air Quality Study

The southern California air quality study (SCAQS), conducted during the summer and fall of 1987 in California's South Coast Air Basin, is the largest air pollution study carried on in southern California [*Lawson*, 1990]. SCAQS focused both on summer episodes exhibiting high levels of secondary pollutants such as ozone and fine particulates, and autumnal events with high concentrations of primary pollutants such as CO and NO_x. There were 11 intensive sampling days in the summer period, covering five separate episodes, and 6 days in the fall, covering three episodes. During the summer events, 36 surface stations reported hourly concentrations of O_3, NO, NO_x, CO, and SO_2, in addition to 24-hour-averaged measurements of PM10, as well as particulate sulfates and nitrates. Of these surface stations, two sampling locations were heavily instrumented, while nine sites were equipped only with the basic SCAQS aerosol and gas samplers. Surface meteorological data were collected at SCAQS sampling sites and at other locations throughout the basin. Daily upper air soundings were taken at six rawinsonde and two airsonde sites during the summer period. Aircraft provided measurements of O_3, NO_x, SO_2 in the upper air layers, as well as lidar images of aerosol backscatter intensity. A layout of the SCAQS network and sampling stations is shown in Figure 1. The SCAQS data archived for the air pollution episode of August 26-30, 1987, is employed here to evaluate the performance of the SMOG model. This archive contains three databases: surface air quality data; surface meteorological data; and upper air measurements collected from a variety of sources, including routine and focused observations during the period [see *California Air Resources Board (CARB)*, 1990].

A series of atmospheric tracer dispersion experiments were conducted during the SCAQS period [*England and Marsh*, 1992]. Four perfluorocarbon tracers were released to tag air movement in the basin. These tracers are perfluoromethyl cyclopentane (PP-1/2), perfluoromethyl cyclohexane (PP-2), perfluorodimethyl cyclohexane (PP-3), and perfluorotrimethyl cyclohexane (PP-4). A fixed surface sampling network was used to collect air parcels that were analyzed for tracer

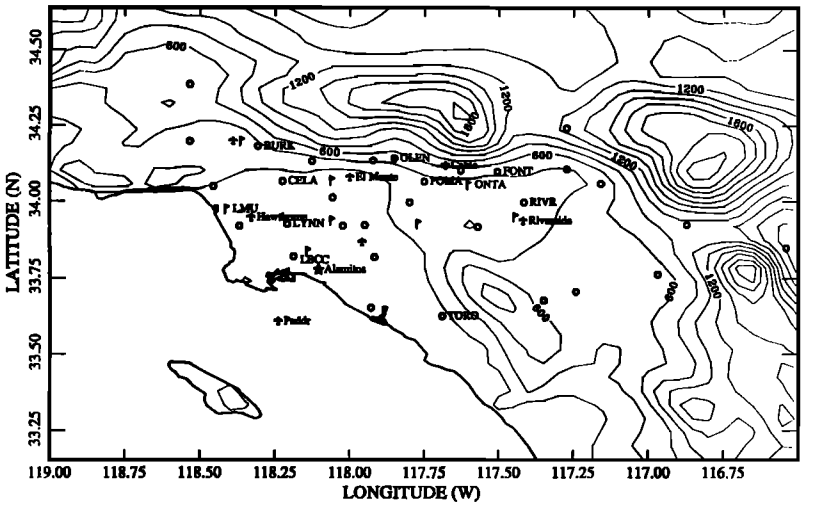

Figure 1. Configuration of the SCAQS observational network and locations of some of the measurement stations within the Los Angeles basin. Contour lines indicate terrain elevation at intervals of 200 m. The coastline of southern California is obvious as the heavy contour in the figure. (Symbols: flag, upper sounding stations; circle, surface measurement stations; star, tracer generating station; airplane, aircraft spiral locations.)

concentration levels. On August 28, tracers were released at Southern California Edison's Alamitos Generating Station. A surface release of PP-3 and a stack release of PP-4 were carried out from 6:00 to 10:00 PST, and a surface release of PP-2 and a stack release of PP-1/2 were carried out from 10:00 to 15:00 PST. Because high background levels of PP-4 were detected prior to the experiment, these data are questionable [*Chico et al.*, 1990]. Tracer data collected at 40 sampling sites distributed across the Los Angeles basin are compared with model predictions in section 3.3.

Spatially and temporally resolved emission fluxes are also needed for air quality simulations. The California Air Resources Board (CARB) emission inventory for August 26-28, 1987, is used in this study [*Allen and Wagner*, 1992]. For gaseous species, gridded hourly emissions are provided for CO, NO_x (NO, NO_2 and HONO), SO_x (SO_2 and SO_3), and reactive organic gases (ROGs), including nonmethane hydrocarbons (NMHCs). Specifically, the ROGs include formaldehyde, ethene, methanol, ethanol, isoprene, and carbon-bond-IV surrogates, that is, paraffins (PAR), olefins (OLE), high molecular weight aldehydes (ALD2), toluene (TOL), and xylene (XYL). Stack emissions are distinguished from surface emissions in the inventory. A plume rise model is used to treat stack emissions, as discussed in paper 1.

The mobile sources in the CARB emission inventory were estimated with a detailed vehicle emission factor model (EMFAC7 [*CARB*, 1991]). However, highway tunnel experiments conducted for SCAQS [*Ingalls et al.*, 1989] suggest that the CO and NMHC emissions from on-road vehicles are significantly underestimated by the EMFAC7 code [*Pierson et al.*, 1992]. In their simulations, *Harley et al.* [1993] increased the on-road vehicle hot exhaust emission rates for CO and organic gases in the CARB inventory by a factor of 3. *Jacobson* [1994] and *Jacobson et al.* [1996a] adjusted the on-road hot exhaust emission inventory of organic gases upward by a factor of 3, and the total CO emission inventory by a factor of 1.6. However, predicted ozone concentrations were still systematically lower than observed concentrations. Uncertainties in other vehicular emissions and stationary sources may have contributed to these under-predictions of ozone.

Fujita et al. [1992] compared the ratios of CO, NMHC, and NO_x in the emission inventory and ambient concentrations in the Los Angeles basin. The ambient ratios of 20 for CO/NO_x and 8.8 for NMHC/NO_x (mol *C*/mol NO_x) in the SCAQS summer study were derived from measurements in the early morning (7:00 to 8:00 PST) corresponding to peak commuter traffic while at the same time preceding significant photochemical activity. The observed CO/NO_x and NMHC/NO_x ratios were about 1.5 and 2-2.5 times greater, respectively, than the corresponding ratios in the CARB emission inventory. Assuming that the NO_x emissions in the CARB inventory are reasonably accurate, and that the measured ambient ratios approximately represent those in the actual emissions, the CO and NMHC emissions in the CARB inventory need to be adjusted accordingly.

In this study the NMHC/NO_x ratios reported by *Fujita et al.* [1992] for each morning of the SCAQS project were used to adjust emissions. First, the on-road hot exhaust emissions of organic gases were increased by a factor of 3, and the total CO emission was increased by a factor of 1.6, in accordance with earlier work [e.g., Jacobson *et al.*, 1996a]. Then a third factor was applied to bring the total emissions of organic gases in the regional inventory into agreement with the ratio of 8.8 for NMHC/NO_x. Table 1 gives the adjusted total daily emissions for August 27 and 28. Obviously, this modified inventory is not an exact representation of the actual sources of primary pollutants in the Los Angeles basin, but it is a reasonable first-order approximation. Further research is needed to reduce uncertainties in primary emission rates.

3. Model Simulations for SCAQS

3.1. Setup and Initialization

The model computational domain and surface topography are illustrated in Figure 2. The southern California area of

Table 1. Summary of the Adjusted Emission Inventory for August 27 and 28, 1987

Species Name	Emission Rate 10^3 kg/d	
	August 27	August 28
CO	8556	8557
NO	723	727
NO_2	124	125
HONO	6	6
Total NO_X (as NO_2)	1239	1246
SO_2	107	107
SO_3	4	4
Total SO_X (as SO_2)	110	110
C_2H_4	241	241
CH_2O	60	60
Aldehyde-2	95	96
Paraffin	1985	1989
Olefin	157	159
Toluene	378	378
Xylene	301	301
CH_3OH	9	9
CH_3CH_2OH	48	48
Isoprene	83	91
Total NMHC	3357	3372

interest is covered by an 85×55 grid system with spacing of 0.050° longitude (4.6 km) and 0.045° latitude (5 km). Lying within this meteorological domain, the air quality computational grid contains 51×34 cells covering the Los Angeles basin and adjacent areas. Twenty nonuniform vertical layers with the highest resolution near the surface are used for both models in the present simulations (refer to paper 1 for details). Upper air soundings taken around 4:00 PST are used to initialize the meteorological grid each day of the simulation (the procedure is described in paper 1). To incorporate changes in the large-scale forcing and to eliminate errors accumulated in the model domain, we reinitialize the meteorological fields each morning in the present simulations. At the edge of the domain, open boundary conditions are adopted, and boundary winds are "nudged" using large-scale flows, as discussed in paper 1.

A multilayer hybrid boundary layer model is used to calculate vertical fluxes of heat and moisture. Accordingly, subgrid scale convective processes and turbulence are parameterized in the transport model (paper 1; also *Lu and Turco* [1994]). A 10-layer soil model predicts subsurface heat transfer and moisture content (the first soil layer is 0.5 cm thick, and the soil is treated to a depth of 1 m; see paper 1). The land surface and soil parameters are assigned uniform values over the domain (Table 2). The initial soil temperatures are assumed to be the same as the initial surface air temperature, and the initial soil moisture content is taken to be 0.16 m^3/m^3. Soil temperature and moisture are initially uniform to a depth of 1 m.

The air quality simulations discussed here are initiated at 4:00 PST on August 26, 1987, and extend for 3 days until 4:00 PST on August 29. The current application of the SMOG model focuses on the gaseous constituents and their photochemistry; aerosol microphysics is not calculated. Table 3 gives the background concentrations for the key primary and secondary species in the simulations. These concentrations apply to relatively clean ambient air outside of the urban zone and provide boundary conditions for the model (in particular, at the upwind inflow boundaries), but otherwise have little impact on the predictions in polluted areas. To initialize the simulations, surface concentrations of O_3, NO, NO_2, CO, SO_2, and NMHC are interpolated from surface measurements at the Air Quality Management District's monitoring network at 4:00 PST, August 26. Because only three NMHC measurements were available at that time, NMHC concentrations at other stations have been estimated using NO_x concentrations as a surrogate, with the assumption that the ratio of NMHC/NO_x (mol *C*/mol NO_x) is 8.8 in early morning (see above; *Fujita et al.* [1992]). The interpolated surface concentrations are extended vertically to the height of the temperature inversion (~970 mbar, or roughly 350 m above sea level) to fill in the initial species distributions

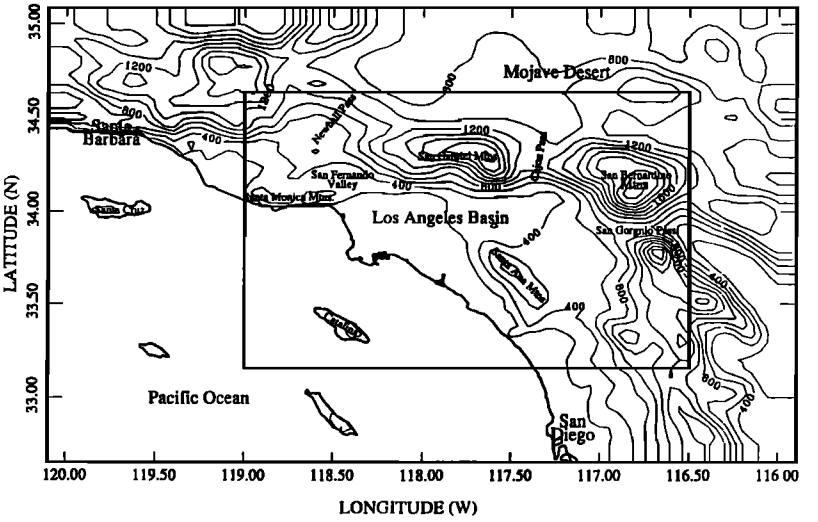

Figure 2. The computational domains and topography adopted for the model simulations are shown. The outer perimeter defines the domain for the meteorological computations. The inner perimeter indicates the subregion in which full chemistry calculations were performed. Terrain is indicated as in Figure 1.

Table 2. Surface and Soil Parameters Adopted in the Model Simulations

Parameter	Value
Surface roughness over land, z_0	0.75 m
Surface roughness over ocean, z_0	0.001 m
Surface albedo, A	0.2
Sea surface temperature, T_{ss}	16° C
Surface emissivity, e_s	0.95
Soil saturated moisture content, W_{sat}	0.435 m^3/m^3
Soil saturated moisture potential, ψ_{sat}	-0.218 m
Soil saturated hydraulic conductivity, K_{sat}	3.41×10^{-5} m/s
Dimensionless exponent for soil, b	4.90
Volumetric heat capacity for dry soil, $\rho_s c_s$	1.34×10^6 J m^{-3} K^{-1}
Volumetric heat capacity for water, $\rho_w c_w$	4.186×10^6 J m^{-3} K^{-1}

within the mixed layer. Above the boundary layer, and over the adjacent ocean, background concentrations are assumed.

These initial conditions, while highly uncertain, are not relevant after the first day of simulation. Indeed, realistic upper-air distributions of chemical tracers are generated by the second day of the model run. Accordingly, only forecasts for the second and third days of the simulations are analyzed.

3.2. Analysis of Meteorological Predictions

On August 27 and 28, 1987 (the second and third days of the simulations), the predominant pressure systems influencing the California coastal region were the eastern Pacific High centered well off the coast and a thermally induced low-pressure cell extending inland from northwestern Mexico to northern California. During the 2 days of interest, the thermal low intensified, increasing the ocean/land pressure gradient and strengthening onshore flow. Within the Los Angeles basin, complex surface wind patterns evolved. On August 27 the flows were primarily westerly, extending from the western coast to the eastern basin, except in Orange County (southern basin; 33.6°N, 117.9°W) where southwesterly flow dominated. On August 28 these southwesterly winds covered a larger region extending from Orange County northward to the San Gabriel Valley (34.20°N, 117.75°W), with predominantly westerly flow near the coast and in the eastern basin.

Table 3. Background Gas Phase Species Concentrations Assumed as Lateral Boundary Conditions in the Simulations

Species	Concentrations (ppbv)
CO	110
NO	0.01
NO_2	1
HONO	0.01
O_3	40
$CH_3CO_3NO_2$	0.05
HCHO	1
C_2H_4	1
PAR	10
OLE	0.1
ALD2	3
TOL	1.1
XYL	0.6
CH_3OH	0.1
CH_3CH_2OH	0.01
ISOP	0.01
CH_4	1650

A strong temperature inversion was evident during the entire period. Figure 3 shows the average vertical profiles of temperature and dew point temperature for the rawinsonde stations within the model domain at 4:00 PST on August 28. The temperature inversion of about 9° C was located between 300 and 900 m above sea level. The lowest ~350 m of the atmosphere was relatively well mixed at this time. On August 29, the lifting of the capping inversion improved basin-wide air quality.

The overall performance of the model was similar on August 27 and 28. Therefore our discussion is confined primarily to August 28, when several passive tracer experiments were also carried out (see section 3.3).

Surface winds. Figures 4a-4c compare observed and predicted surface winds at several times of the day on August 28. At 12:00 PST, the observed winds were onshore in the coastal regions, upslope near the San Gabriel Mountains, and largely eastward along the mountains in the eastern basin. In the central basin, winds were relatively weak. Overall, the predicted winds replicate the observed flow. Analysis of the simulation indicates that developing sea-breezes and mountain upslope currents are responsible for the observed patterns. Even the easterlies in the far eastern region, and a surface convergence at about 117°W, are reproduced. Some smaller scale features in the wind patterns are not captured, including a local northwesterly flow observed north of the Palos Verdes peninsula and hills (33.75°N, 118.35°W) and more southerly winds seen to the east of the peninsula.

The sea breeze and mountain winds are fully developed by midafternoon in both observations and simulations (Figure 4b). Westerlies are seen both in the coastal regions and in the eastern basin. An avenue of southwesterly wind extends inland from the coast of Orange County (~118°W) toward

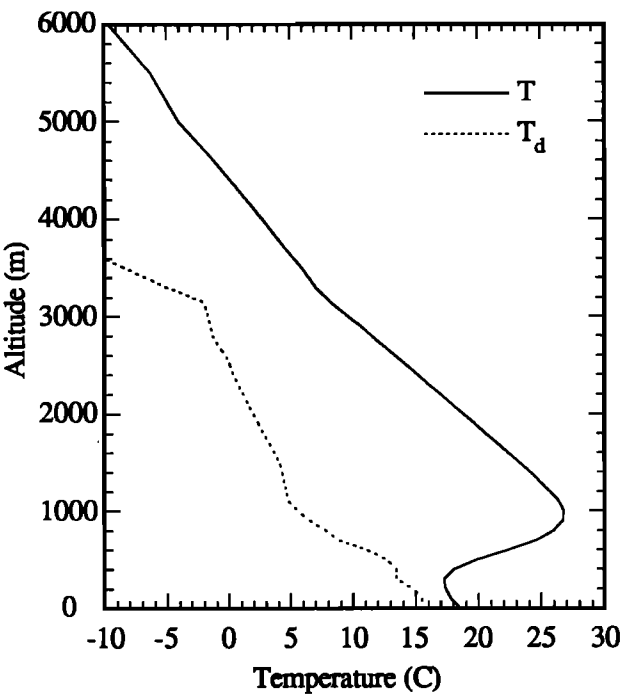

Figure 3. The station composite of potential temperature and dew point temperature profiles at 4:00 PST on August 28, 1987.

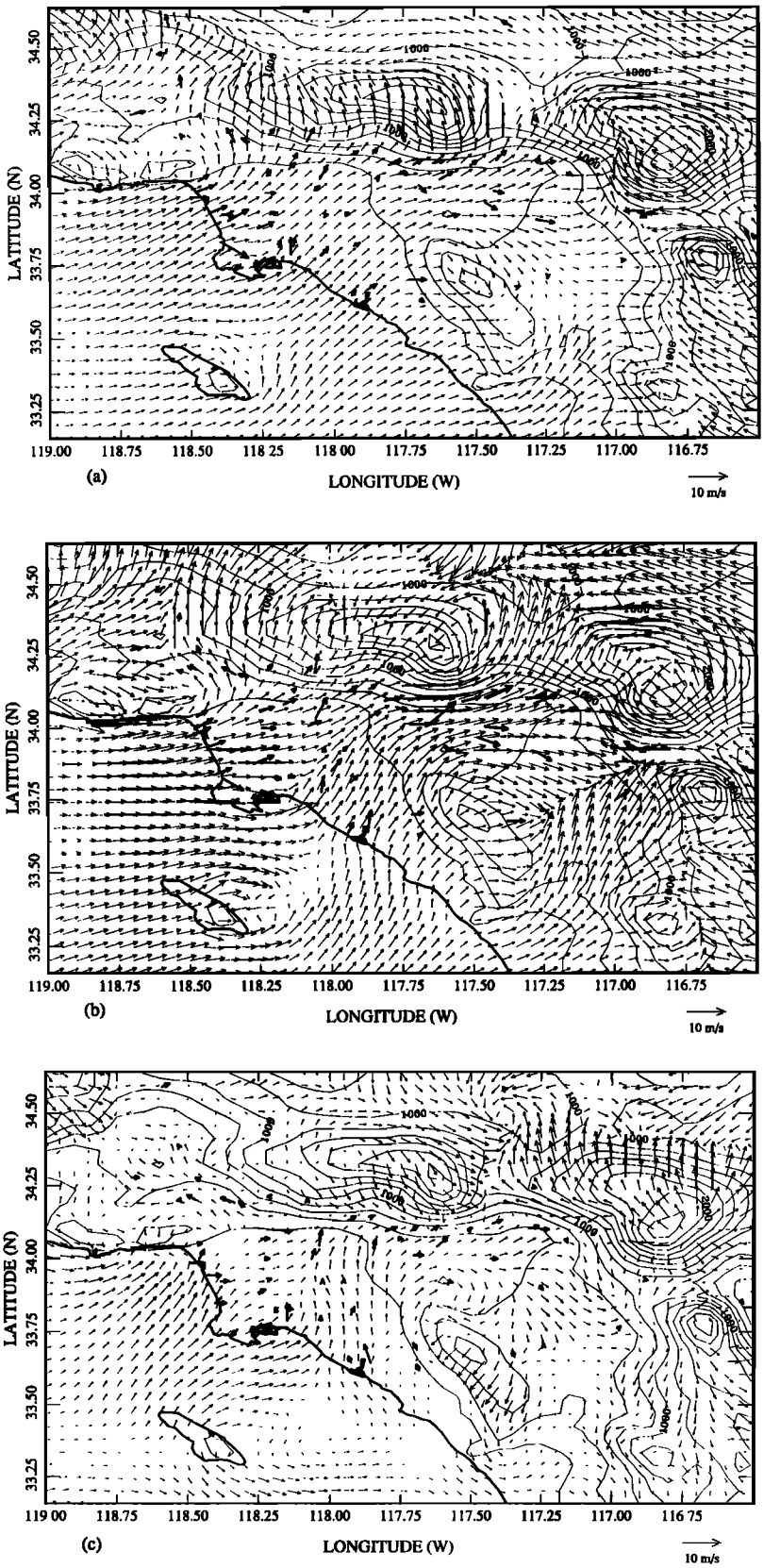

Figure 4. Predicted and observed surface wind vectors on August 28, 1987. The heavy arrows are the observations, while the light arrows define the predicted surface wind field at (a) 12:00 PST, (b) 16:00 PST, and (c) 20:00 PST.

Pomona to the north. In the San Fernando Valley (34.2°N, 188.6°W), southeasterly flow is predicted to converge with westerly flow across the Oxnard plain (119°W), as recorded in measurements. The model simulations also show surface air moving up the southern flank of the San Gabriel Mountains, as had been observed, although predictions of southward flow north of the San Gabriel Mountains are not corroborated by measurements. The proximity of the model boundary to the northern deserts complicates the calculation of surface winds in this remote region. Fortunately, the desert circulations are effectively decoupled by mountain barriers from the surface dynamics of the Los Angeles basin. Air transport through regional passes to the north and east of the basin, on the other hand, are correctly represented in the simulations. For example, observed easterlies across the Banning pass (San Gorgonio; 33.85°N, 116.80°W) and southerlies through the Cajon pass (34.25°N, 117.3°W) and Newhall pass (34.5°N, 118.6°W) are also found in the simulations.

The onshore and inland air flow within the basin continues into the evening hours, with wind speeds decreasing and becoming stagnant by midnight (Figure 4c; 20:00 PST). Model predictions track the overall changes in wind patterns observed during the nocturnal period, although with decreasing fidelity as variable surface winds and drainage flows develop. The drainages tend to be localized and thus difficult to reproduce owing to the influence of small-scale terrain variations, which are not present in the relatively smooth gridded SMOG topography. The smoothness, in fact, tends to enhance drainage from the mountain slopes.

On August 27, winds in the basin had generally been more westerly throughout the day than those on August 28. Shifts in wind patterns between August 27 and 28 were driven by changes in the large-scale surface pressure distribution. Further, evolution of the upper-level winds and geostrophic flow also modified air currents over the local mountain ranges during this period. Overall, the predicted surface winds in the Los Angeles basin on August 27 agree with observations as well as those on August 28 (see section 3.2, statistical evaluation, below).

Vertical temperature profiles. Predicted vertical temperature profiles are generally consistent with upper air soundings. The inland station at Ontario (ONTA; refer to Figure 1) represents the situation in the central and eastern basin. Figures 5a-5f compare observed and predicted vertical profiles of potential temperature at Ontario on August 28. In the early morning the lowest 400 m of the atmosphere is strongly stable. The boundary layer temperature rises during the morning hours, and the mixed layer depth increases. At 10:00 and 13:00 PST the calculated mixed layer temperature is slightly cooler than observed, and the mixed layer depth is somewhat shallower than measured. By 16:00 PST, the mixed layer temperature is precise, but the mixed layer depth is overpredicted. During the nocturnal period (21:00 PST and 4:00 PST), the decrease in surface temperature is accurately predicted, although the lower atmosphere is somewhat more stable than observed.

In the coastal regions, such as at Loyola Marymount University (LMU) and Long Beach Civic Center (LBCC; refer to Figure 1), the boundary layer is strongly influenced by the intrusion of marine air. Stratus clouds were reported over these stations during the simulation period, and water vapor saturation was detected at the top of marine mixed layer. Boundary layer cloud formation is not explicitly included in the results discussed here. Hence sharp discontinuities observed in the vertical temperature profile at the top of the marine layer are not reproduced in the model. This shortcoming can readily be dealt with using the parameterization scheme discussed in paper 1. The implications for the present simulations are minimal, however, because marine clouds existed only over a limited coastal area during the period of interest. Above the temperature inversion, measured changes in air temperatures were small on August 28, and the SMOG simulations yielded values to within roughly 1 K.

Vertical wind profiles. Figure 6 displays observed and predicted vertical wind profiles at the ONTA and LMU stations on August 28. Over Ontario at 10:00 PST, a shallow southwesterly flow was noted at the surface, which veered toward the west and northwest aloft. At 13:00 PST, the winds in the boundary layer were westerly but turned sharply toward the north, and then veered easterly, above the mixed layer. The model accurately reproduces these wind speeds and directions throughout the lower troposphere. By 16:00 PST the westerly boundary layer flow expanded to a height of about 1.5 km, a feature that is also captured in the simulation (Figure 6c).

Over LMU, weak variable surface winds intensified toward the east between morning and afternoon. Above the boundary layer, winds were generally easterly, and also increased during the day. These striking features in the wind structure are faithfully reproduced in the model simulations (Figures 6d and 6e). In the evening hours, winds below 1.5 km were again weak and variable. However, between 1.5 and 5 km, easterlies dominated the flow, as replicated in the calculations.

Statistical evaluation. To evaluate model performance quantitatively, a set of standard statistical measures can be computed [*Keyser and Anthes*, 1977; *Willmott et al.*, 1985]. These measures are defined as follows:

$$\sigma_p = \left[\frac{1}{N}\sum_{i=1}^{N}(\mathbf{p}_i - \bar{\mathbf{p}})^2\right]^{1/2} \quad (1)$$

$$\sigma_o = \left[\frac{1}{N}\sum_{i=1}^{N}(\mathbf{o}_i - \bar{\mathbf{o}})^2\right]^{1/2} \quad (2)$$

$$\mathrm{RMSD} = \left[\frac{1}{N}\sum_{i=1}^{N}(\mathbf{p}_i - \mathbf{o}_i)^2\right]^{1/2} \quad (3)$$

Here σ_p and σ_o are the standard deviations of predicted and observed values of a relevant parameter, respectively, given data at N sites or locations. The parameters $\mathbf{p}_i$ and $\mathbf{o}_i$ may be vector or scalar quantities taken as hourly average values at each specific location i, where $\bar{\mathbf{p}}$ and $\bar{\mathbf{o}}$ are the mean values for the N locations. Further, the root-mean-square difference (RMSD) between the predictions and observations is defined by (3). The skill level of the model prediction is considered to be high if the standard deviation of the predictions is comparable to that of the observations, while the root-mean-square difference is smaller than the standard deviation of the observations [Pielke, 1984]. Following *Willmott et al.* [1985], RMSD between predictions and observations is decomposed into two components, specifically, the systematic root-mean-square difference (RMSD_s) and the unsystematic root-mean-square difference (RMSD_u):

$$\mathrm{RMSD}_s = \left[\frac{1}{N}\sum_{i=1}^{N}(\hat{\mathbf{p}}_i - \mathbf{o}_i)^2\right]^{1/2} \quad (4)$$

$$\mathrm{RMSD}_u = \left[\frac{1}{N}\sum_{i=1}^{N}(\hat{\mathbf{p}}_i - \mathbf{p}_i)^2\right]^{1/2} \quad (5)$$

where

$$\hat{\mathbf{p}}_i = a + b\mathbf{o}_i \quad (6)$$

and a and b are the intercept and slope, respectively, associated with the least squares linear regression between **p** and **o**. $(\mathrm{RMSD})^2 = (\mathrm{RMSD}_s)^2 + (\mathrm{RMSD}_u)^2$. RMSD_s is a measure of linear bias in the model predictions, while RMSD_u describes the nonlinear discrepancy between predictions and observations, which may be interpreted as a measure of precision.

An index of agreement between the predictions and observations of a parameter is defined as [*Willmott*, 1981]

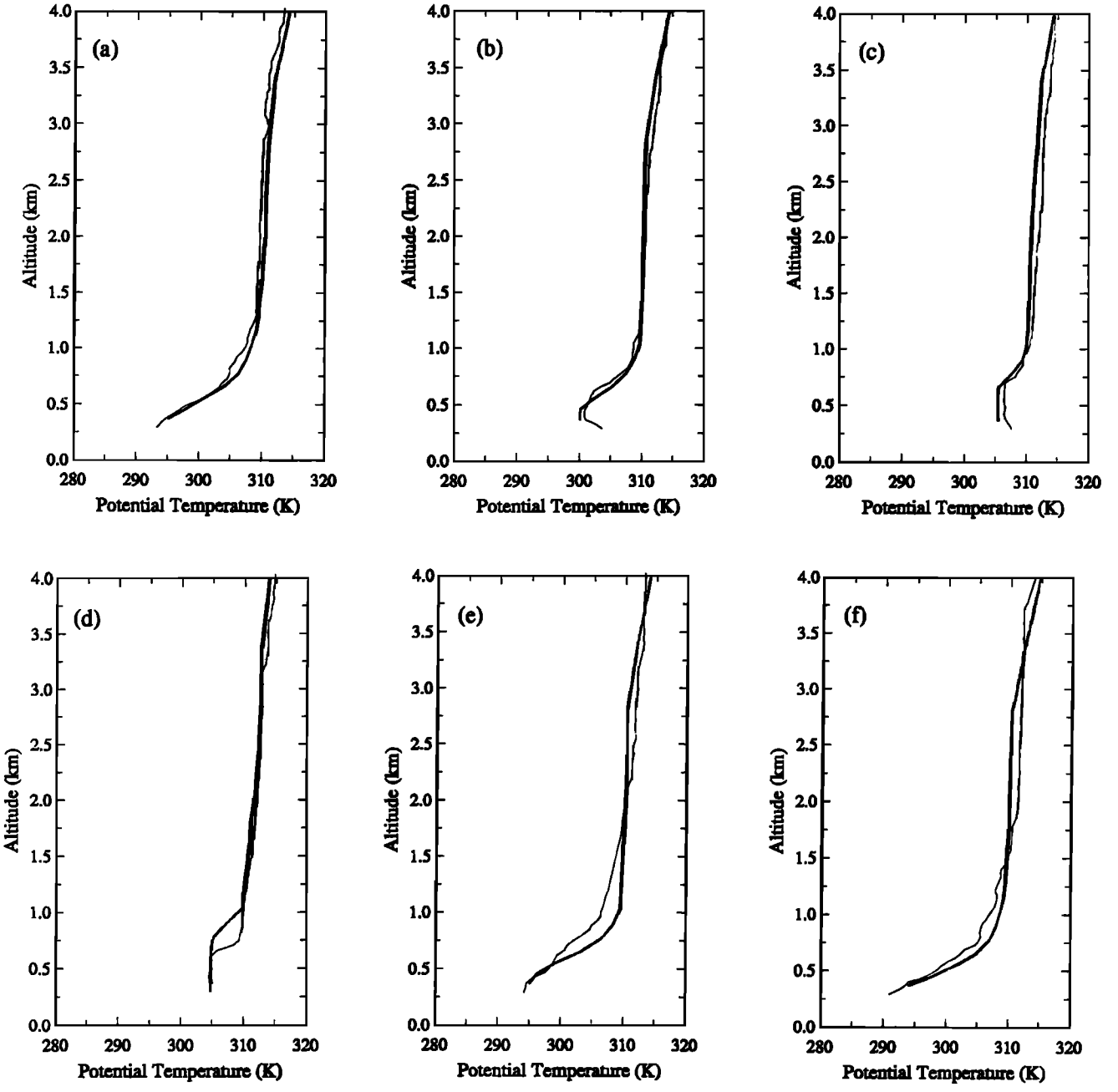

Figure 5. Comparison of predicted and measured vertical profiles of potential temperature for August 28, 1987, at the Ontario, California, station (ONTA; see Figure 1). Light lines represent observations, and heavy lines represent predictions. Altitudes are taken relative to sea level. The base of each sounding corresponds to the local surface elevation, whereas the base of the predicted temperature profiles corresponds to the elevation at the center of model surface layer. The six plots correspond to times of (a) 7:00 PST, (b) 10:00 PST, (c) 13:00 PST, (d) 16:00 PST, (e) 21:00 PST, and (f) 4:00 PST (on August 29).

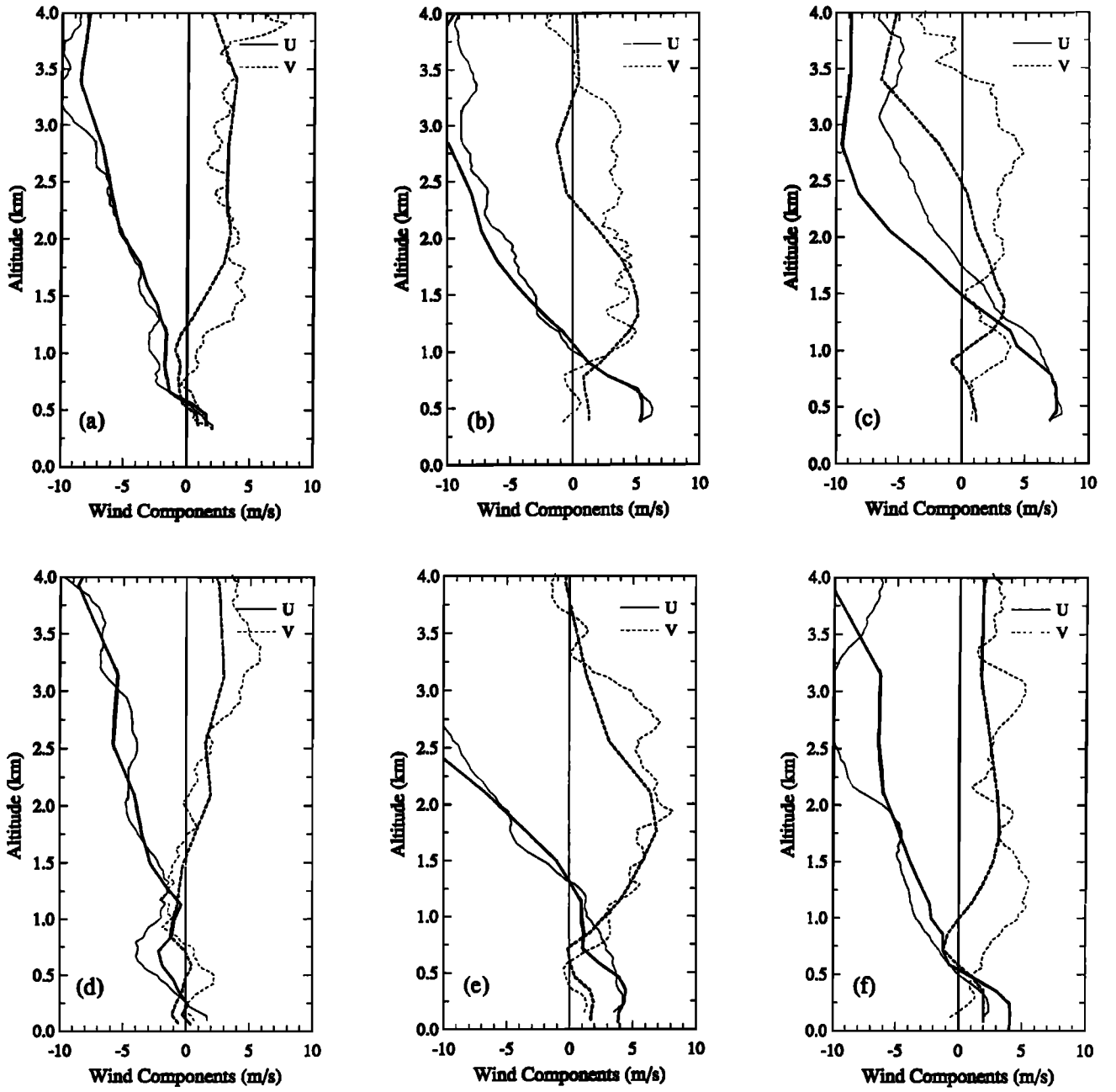

Figure 6. Comparisons of predicted and observed vertical wind profiles for August 28, 1987. Solid lines indicate the u (zonal) component, and dashed lines indicate the v (meridional) component. Light lines represent observations, and heavy lines represents predictions. The locations (refer to Figure 1) and times are (a) ONTA at 10:00 PST, (b) ONTA at 13:00 PST, (c) ONTA at 16:00 PST, (d) LMU at 7:00 PST, (e) LMU at 13:00 PST, and (f) LMU at 16:00 PST.

$$I = 1 - \frac{\sum_{i=1}^{N} (p_i - o_i)^2}{\sum_{i=1}^{N} \left(|p_i - \bar{o}| + |o_i - \bar{o}| \right)^2} \quad (7)$$

This index compares the departure of predictions from the mean value of observations with the departure of the individual observations from the mean [*Ulrickson and Mass*, 1990]. The possible range of I is 0 to 1, where the latter score suggests perfect agreement.

Figures 7 and 8 present a statistical assessment of predicted and observed surface winds for each hour on August 27 and 28, 1987. The observed surface winds were obtained as hourly average values measured at several dozen sites throughout the Los Angeles basin. At each observational site, the predicted wind components correspond to those present in the lowest model layer for the grid cell containing the site and are averaged over 1-hour intervals based on a fully time-dependent calculation.

The overall modeled and observed mean surface wind speeds and directions are in close agreement on both days

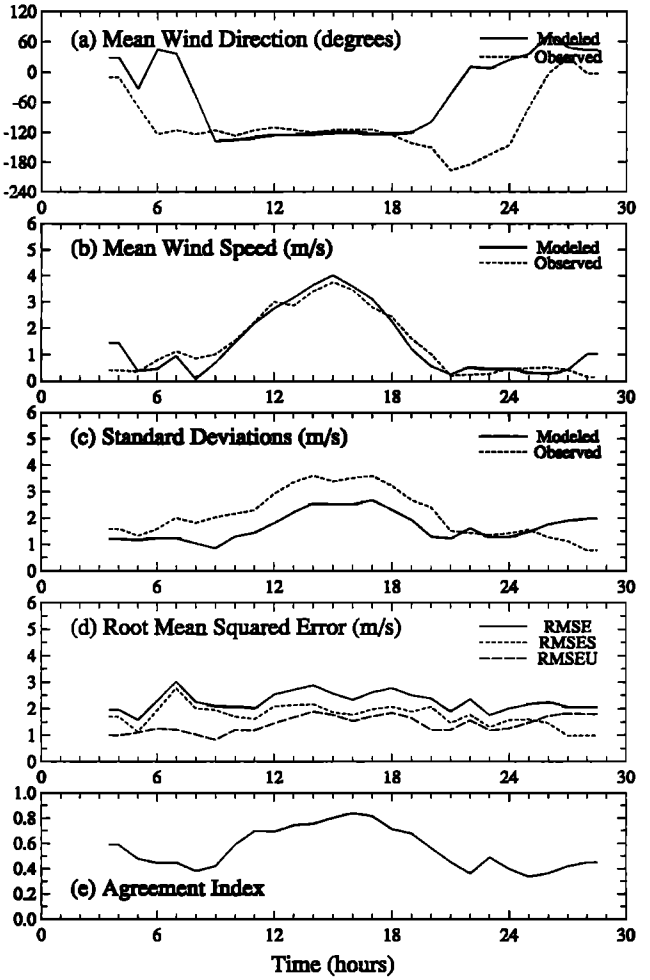

Figure 7. Comparison of predicted and observed surface winds for August 28, 1987. The individual curves in each panel are identified in the legends. The parameters illustrated are (a) the mean wind direction (degrees, from due north), (b) mean wind speed (m s^{-1}), (c) standard deviation of wind field (m s^{-1}), (d) vector root-mean-square difference (m s^{-1}), and (e) the agreement index, defined in the text.

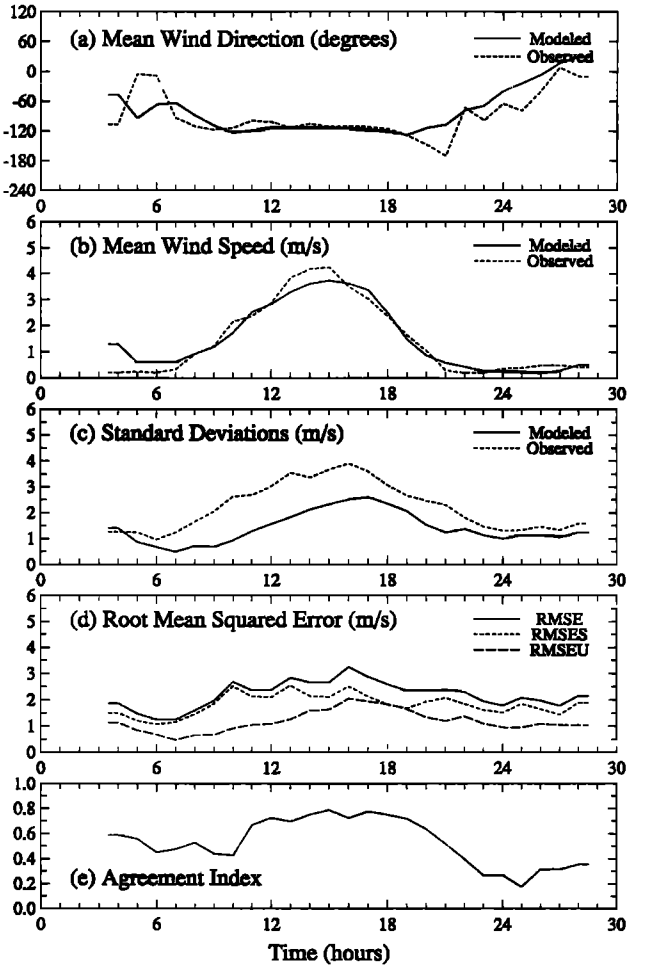

Figure 8. Comparison of predicted and observed surface winds for August 27, 1987. The individual curves in each panel are identified in the legends. The parameters illustrated are (a) the mean wind direction (degrees, from due north), (b) mean wind speed (m s^{-1}), (c) standard deviation of wind field (m s^{-1}), (d) vector root-mean-square difference (m s^{-1}), and (e) the agreement index (see the text).

(Figures 7a, 7b and 8a, 8b). The differences in mean speed are within 0.5 m/s. In the case of the mean wind direction, the simulations are quite accurate during the daytime. Major differences, however, occur during the night when the wind speeds are small and the flow becomes disorganized. During daylight, the standard deviations of the predictions are smaller than those of the observations, and the RMSDs are about 1 to 3 m/s. However, the agreement indices, which have peak values of about 0.85 during midday, indicate that the overall simulated patterns of surface winds are in good agreement with observations, although the predicted spatial variability is somewhat smaller. The degree of spatial correlation and variability in the observations and simulations can also be judged qualitatively in Figure 4. The predicted surface winds are smoother than the observed winds (that is, they have a lower standard deviation; Figures 7c and 8c), because the horizontal resolution of the model is too coarse to represent small-scale phenomena that are likely to affect actual winds. At night, light and variable surface winds are also more likely to be influenced by local terrain features.

The statistical measures for simulated and observed surface air temperatures are shown in Figure 9 for August 28. The mean temperatures are in excellent agreement, except during the first 3 hours when an adjustment to the daily reinitialization of lower-level air and surface temperatures occurs (see paper 1). As with the surface winds, the simulated surface temperatures show less variability than observations (smaller standard deviation; Figure 9b). Inhomogeneities in local surface properties, which are not included in the model, may contribute to the differences between predicted and measured temperature variability. During the daytime the RMSD is smaller than the standard deviation of the observations. Moreover, the index of agreement, which is as large as about 0.9, indicates that the model is accurately replicating the observed patterns of surface temperatures.

The comparisons between model predictions and observations on August 27 and 28 indicate that the SMOG model is capable of simulating accurately the general features of the meteorology of the Los Angeles basin. Statistical

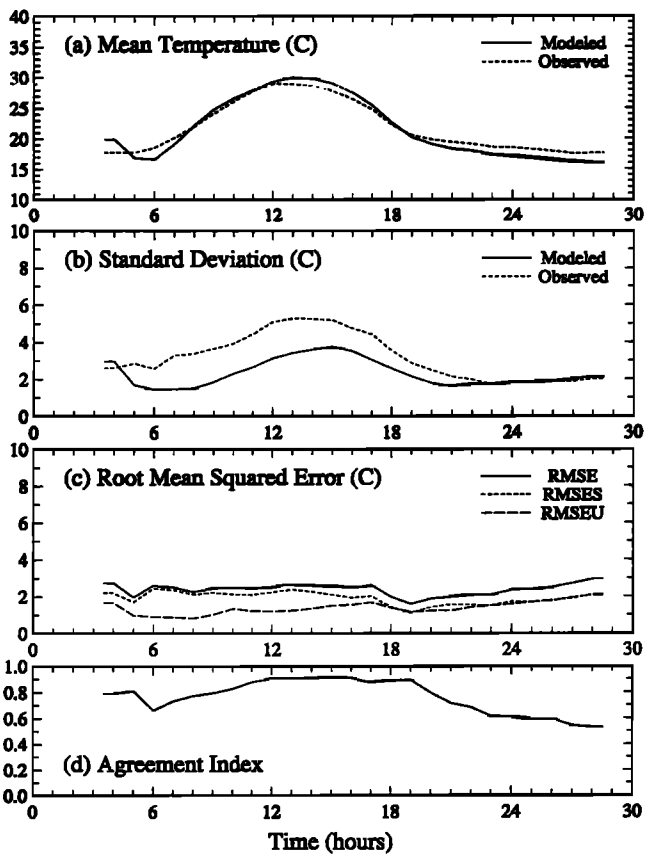

Figure 9. Comparison of predicted and observed surface temperatures for August 28, 1987. The individual curves in each panel are identified in the legends. The panels illustrate (a) the mean surface temperature (°C), (b) the standard deviation of the field (°C), (c) root-mean-square difference (°C), and (d) the agreement index (see the text).

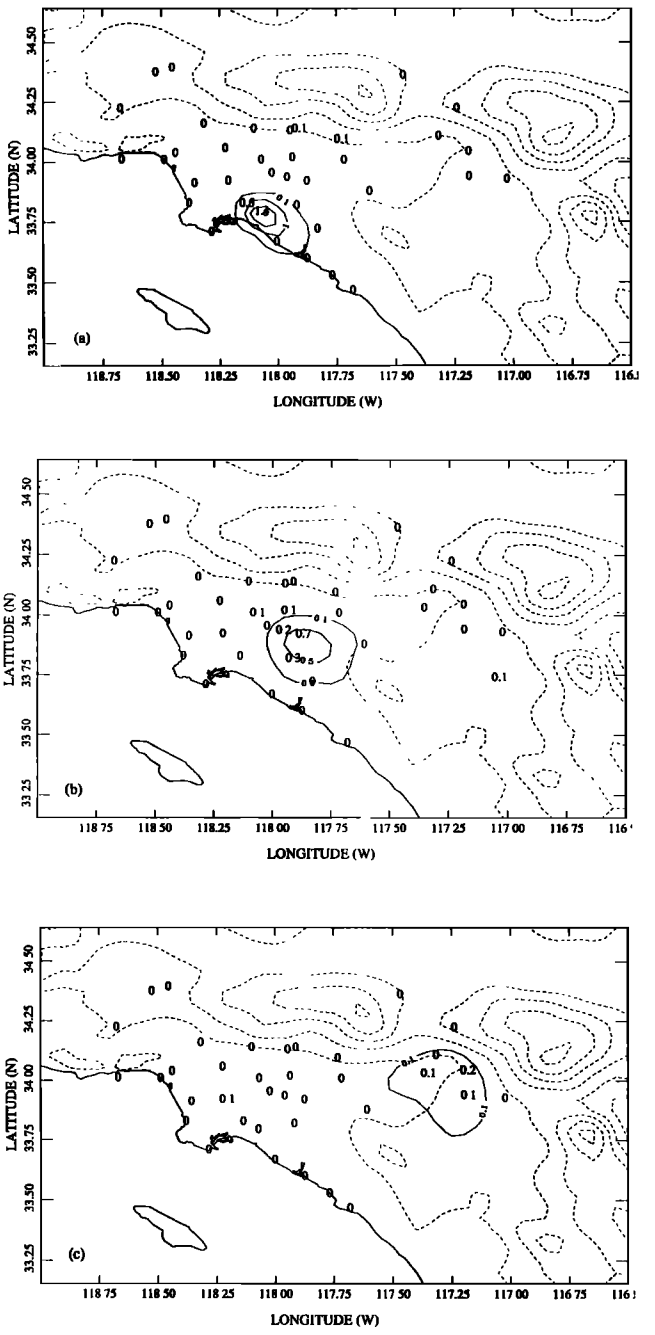

Figure 10. Predicted and observed surface concentrations of tracer PP-3 (perfluorodimethyl cyclohexane) on August 28, 1987. The solid contours represent the model predictions (parts per trillion by volume, pptv), while observed concentrations are indicated at sampling locations by bold numerals (pptv). The panels correspond to (a) 10:00 PST, (b) 13:00 PST, and (c) 16:00 PST.

evaluation of the simulations also demonstrate significant skill for predicting key parameters such as surface winds and boundary layer structure. These forecasts can be further assessed using the tracer transport data, as is done below.

3.3. Tracer Transport Analysis

In this section the SMOG model is used to simulate tracer experiments conducted on August 28, 1987. The tracers were released at the Alamitos Generating Station (118.105°W, 33.781°E). PP-3 was released from 6:00 to 10:00 PST; PP-2 and PP-1/2 were released from 10:00 to 15:00 PST. Since the stack release of PP-1/2 yielded transport patterns very similar to those for the concurrent surface release of PP-2, only the PP-2 (and PP-3) results are discussed in detail. In the model these tracers are injected at the surface within the corresponding model grid. Predicted tracer concentrations in the lowest model level are then compared with measured near-surface concentrations (upper air measurements are not available for these experiments).

Surface tracer concentrations. Calculated and observed PP-3 surface concentrations at different times of the day are shown in Figure 10. At 10:00 PST, both the observed and simulated tracer plumes remain close to the release point (Figure 10a). Small concentrations of PP-3 detected on the southern slopes of the San Gabriel mountains far to the north are likely due to other sources or to contamination. By 13:00 PST (Figure 10b) the tracer plume has moved northward into the central basin. At 16:00 PST the tracer has been transported well into the eastern basin (Figure 10c). The model simulations replicate the transport patterns and tracer concentrations very well.

Figure 11 shows computed and measured PP-2 surface concentrations during the tracer experiments. Measurements

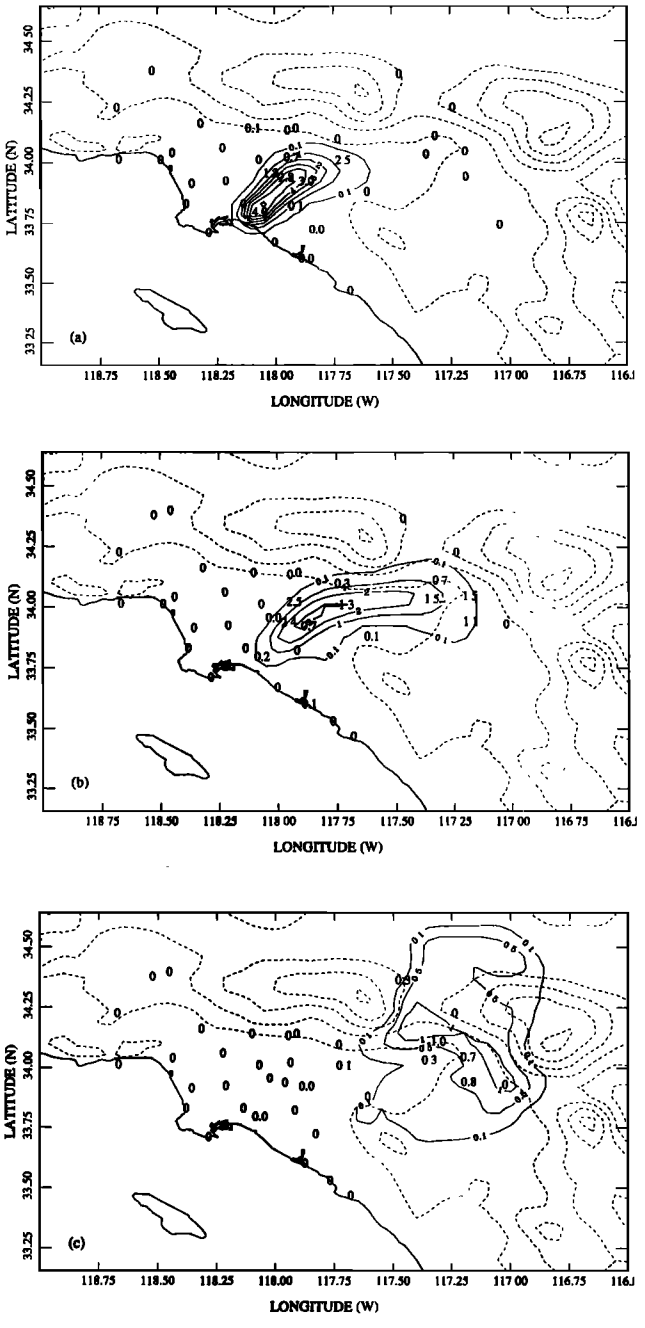

Figure 11. Predicted and observed surface concentrations of tracer PP-2 (perfluoromethyl cyclohexane) on August 28, 1987. The solid contours represent the model predictions (pptv), while observed concentrations are indicated at sampling locations by bold numerals (pptv). The panels correspond to (a) 14:00 PST, (b) 16:00 PST, and (c) 20:00 PST.

carried out prior to noon (not illustrated) show that the injected material remained near the source, initially moving slowly toward the northeast. By 14:00 PST the PP-2 had been transported eastward across the Puente Hills into the eastern basin (Figure 11a). This northeastward and then eastward transport of the tracer is reproduced by the model. However, the head of the tracer plume is transported at a somewhat slower rate than measurements suggest. In the afternoon, however, the PP-2 moves much faster and reaches the eastern end of the basin by 16:00 PST (Figure 11b), as observed. Although the model reproduces this fast eastward transport in midafternoon, the observed location of a second tracer peak in the eastern basin is not achieved, in part because of the delay in the morning. By late afternoon, the tracer has been transferred to the San Bernardino area in the northeast. Although the measurement network was not dense enough to define the tracer distribution fully in this region, both the observations and simulations suggest that the tracer remained in the eastern basin during the night. Predictions of tracers to the east of the Santa Ana Mountains (Figure 11c) could not be confirmed by observations.

Tracer transport through Cajon Pass. An important feature of the PP-2 measurements is the distinct transport through the Cajon Pass (34.25°N, 117.3°W). The tracer was detected northward of the Cajon Pass between 19:00 PST and 1:00 PST the next morning, with a peak abundance at 21:00 PST [*Chico et al.*, 1990]. The urban airshed model (UAM) did not predict this transport [*Chico et al.*, 1990]. However, in the SMOG simulation, the movement of PP-2 through Cajon Pass is quite evident (Figure 11c). By 18:00 PST, PP-2 begins to move into the Cajon Pass. From 18:00 to 23:00 PST, a surface parcel separates from the main plume in the eastern basin, moving to the high desert region through the pass. The simulated tracer plume appears broader and farther eastward than that detected at two sampling stations nearby. This discrepancy in the details is probably related to the smoothing character of the model terrain.

The simulated surface tracer transport patterns are in excellent accord with observations. The northeastward transport in the early afternoon, and subsequent eastward movement, are captured by the simulation, as is transport through the Cajon Pass. The consistency between predicted and observed tracer patterns again demonstrates the fidelity of the meteorological simulations.

3.4. Analysis of Air Quality Predictions

In this section, predictions for ozone and other chemical species on August 27-28, 1987, are discussed. The calculated concentrations of ozone and several key precursor compounds are compared with measurements. The simulations were carried out over a period of 3 days beginning at 4:00 PST, August 26 (and lasting until 4:00 PST, August 29). However, the present analysis focuses on August 27 and 28, when the assumptions used to initialize species concentrations had little influence on the solutions.

Surface ozone concentrations. The observed peak ozone concentrations in the Los Angeles basin typically occur in midafternoon. Figures 12 and 13 illustrate the spatial distributions of ozone at 15:00 PST on August 27 and 28, respectively. The measured 1-hour average ozone concentrations from 14:00-15:00 PST are also given for comparison. On August 27 the pattern of surface ozone showed increasing abundances from the western coastal area toward the northern and eastern regions of the basin. An ozone peak of 24 parts per hundred million by volumn (pphmv) was observed at Riverside-Rubidoux (RIVR in Figure 1). The SMOG simulation remarkably reproduces both the overall spatial distribution and peak values of ozone on this day. However, the predictions differ in many details from the observations. For example, on August 27 the simulated ozone concentration peak, while of the right magnitude,

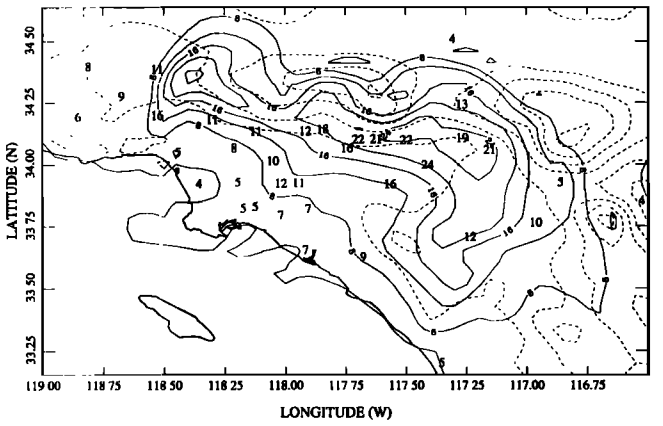

Figure 12. Surface ozone concentrations on August 27, 1987, at 15:00 PST. Solid contours are predicted isopleths of ozone (in pphmv; the contours correspond to intervals of 4 pphmv and are marked at 8, 16, and 24 pphmv). The larger bold numerals on the figure indicate observed 1-hour-average surface ozone concentrations (also in pphmv) for the time period 14:00-15:00 PST. The dashed contours show topographic elevation at intervals of 400 m.

appears eastward of the observed location. On August 28 (Figure 13), the measured ozone maximum was as high as 29 pphmv at the Glendora station in the San Gabriel Valley (GLEN in Figure 1), which is higher than the calculated peak in the same location and a second peak predicted tens of kilometers to the east. Nevertheless, the forecast error of highest ozone abundances was within about 10% of the observed values, and the overall distribution exhibited a root-mean-square error of only about 25-30% over the entire basin (see below).

A secondary afternoon maximum in ozone is predicted in the San Fernando Valley in Figures 12 and 13. Although this feature is not seen in the station data at that time, the simulated surface ozone distributions are nevertheless in

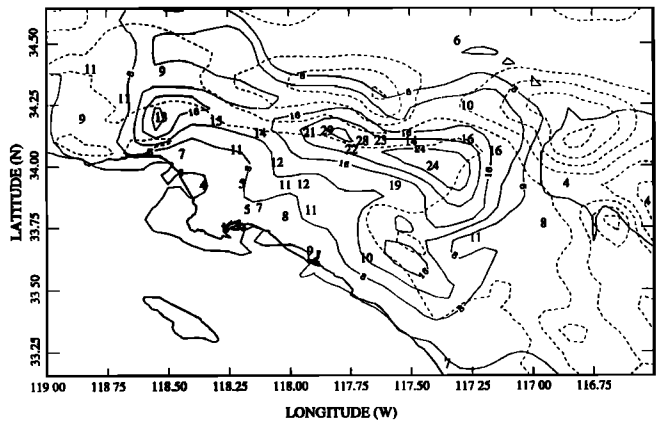

Figure 13. Surface ozone concentrations on August 28, 1987, at 15:00 PST. Solid contours are predicted isopleths of ozone (in pphmv; the contours correspond to intervals of 4 pphmv and are marked at 8, 16, and 24 pphmv). The larger bold numerals on the figure indicate observed 1-hour-average surface ozone concentrations (also in pphmv) for the time period 14:00-15:00 PST. The dashed contours show topographic elevation at intervals of 400 m.

reasonable agreement with the measurements. Comparing the ozone patterns on August 27 and 28, the model is found to capture the evolution of the surface ozone pattern during this episode, which is, to a large extent, the result of complex changes in the meteorological state.

Vertical ozone distributions. During the SCAQS experiment, aircraft were deployed to measure vertical profiles of ozone, NO/NO_x, SO_2, light scattering coefficient, temperature and turbulence from the surface to about 1500 m altitude. The profiles were obtained at specific locations (indicated in Figure 1) where the aircraft performed a spiral maneuver. The ozone values, as reported by *Roberts and Main* [1992], are 30-m vertical averages. Three flights were made on August 27, in early morning, at midday and in the afternoon, and several profiles were obtained during each flight. For the afternoon flight, ozone data are only available at Cable Airport.

Selected vertical profiles measured on August 27 are compared to model predictions in Figure 14. The numerical results are taken from the vertical model column that includes the sampling site for the hour closest to the time of the aircraft maneuver. In addition to the results from the SMOG simulations, predictions from the urban airshed model (UAM) are illustrated [*Southern California Air Quality Management District (SCAQMD)*, 1990, 1991; *Roberts and Main*, 1992].

In Figures 14a and 14b, vertical ozone profiles taken during the midday flight (between 11:00 and 11:30 PST) in the western basin over Paddr (an airway intersection over the ocean 15 km south of Long Beach) and at Hawthorne are shown. The measured ozone concentrations near the surface and above 1000 m are in the range of 50 parts per billion by volume (ppbv) at both sites. However, much higher ozone concentrations (120-150 ppbv) were detected in a layer between 300 and 700 m at Paddr, and an ozone peak of more than 160 ppbv was recorded at 500 to 600 m above Hawthorne. Similar ozone layers are predicted by the SMOG model, although the maximum ozone concentrations are 40 to 50 ppbv lower than the measured values. The UAM simulations, by contrast, show an ozone ledge at 500 m elevation over Hawthorne, and no indication of layering at Paddr.

In the eastern Los Angeles basin, high ozone concentrations were measured in the well-mixed boundary layer during the midday and afternoon flights at Riverside and Cable Airport (Figures 14c and 14d). However, at the top of the mixed layer, ozone concentrations decreased sharply to about 50 ppbv. The SMOG simulations reproduce this vertical structure quite accurately at Riverside. On the other hand, at Cable Airport, which is located on the steep southern slopes of the San Gabriel mountains, calculated mixed-layer ozone concentrations are roughly 20% lower than the measurements, and the mixed layer depth is overpredicted. These offsetting effects imply that a roughly correct amount of ozone has been predicted in the SMOG simulation, but that the ozone has been diluted in a somewhat larger volume of surface air. By contrast, the UAM model shows a much deeper boundary layer at both sites and little evidence of the actual vertical structure seen in the ozone distribution.

Time series analysis. Figures 15a-15f present time series of predicted and observed ozone concentrations at selected monitoring stations in the Los Angeles basin (refer to Figure 1 for the station locations). At most of the stations, the predicted magnitude and phase of the diurnal ozone variation

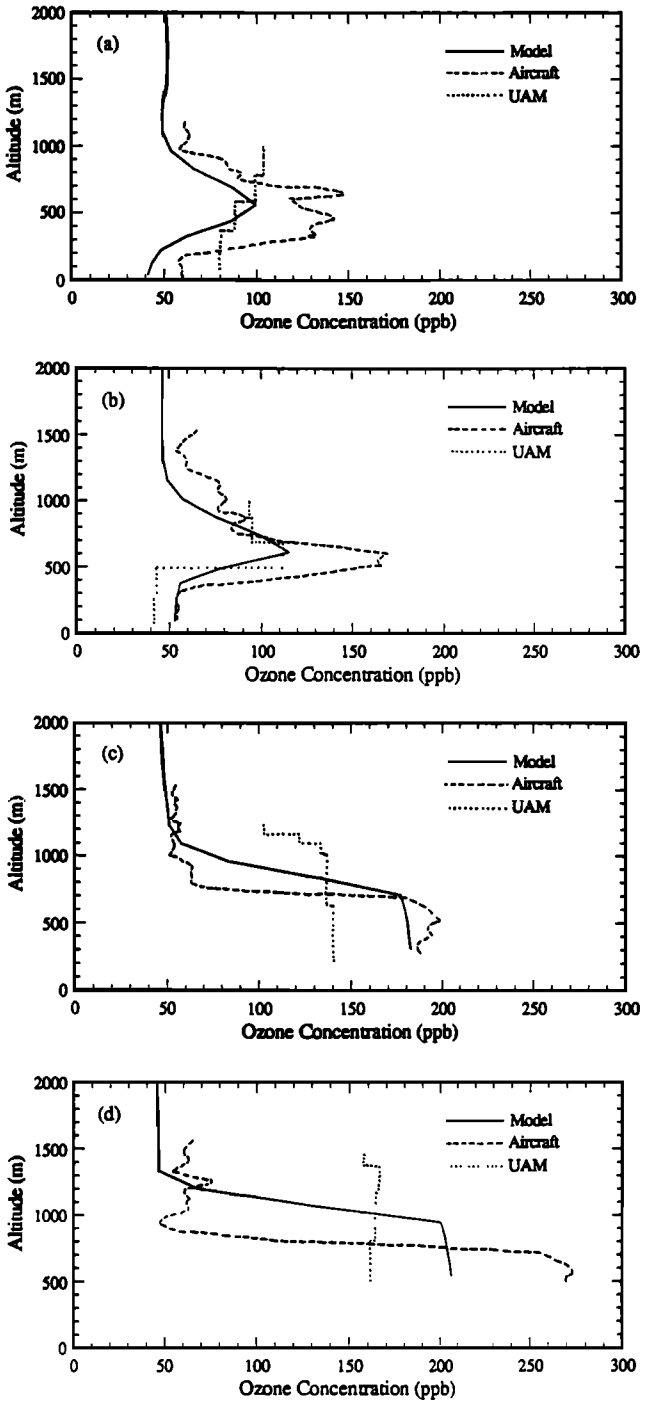

Figure 14. Comparison of observed and predicted vertical ozone profiles on August 27, 1987. Solid lines are model predictions from the SMOG model, dashed lines are aircraft measurements, and dotted lines are predictions from the urban airshed model (UAM). The ozone profiles are shown at four stations (refer to Figure 1 for locations): (a) Paddr, which lies over the water between Long Beach and Catalina Island (model, 12:00 PST; aircraft, 11:24-11:30 PST; UAM, 11:00-12:00 PST), (b) Hawthorne, in the western coastal region (model, 11:00 PST; aircraft, 11:08-11:15 PST; UAM, 11:00-12:00 PST), (c) Riverside, in the central eastern basin (model, 12:00 PST; aircraft, 11:58-12:05 PST; UAM, 12:00-13:00 PST), and (d) Cable Airport, near Pomona (model, 14:00 PST; aircraft, 13:59-14:05 PST; UAM, 14:00-15:00 PST). Aircraft measurements and UAM predictions are taken from *Roberts and Main* [1992].

are in accord with observations. For example, at the central Los Angeles station (CELA), which represents the western region of the basin (Figure 15a), ozone concentrations are typically below about 0.1 parts per million by volume (ppmv) and peak in the early afternoon, as observed. During the SCAQS period, the highest ozone concentration observed was 0.29 ppmv at the Glendora station (GLEN; Figure 15e), where the model underpredicted the peak value by about 15% (although the timing of the peak was quite precise). Indeed, the overall impression from Figure 15 is that the SMOG model performs very well in predicting ozone abundances and variations in polluted areas.

Time series of nitric oxide (NO) and nitrogen dioxide (NO_2) concentrations at the central Los Angeles site (CELA) are provided in Figure 16. The peak NO abundance is observed to appear around 7:00 PST at this location. The SMOG model somewhat underestimates the morning peak value at most stations and delays its occurrence by up to 1-2 hours. Moreover, at some stations, simulated NO concentrations are too large in the evening. Nevertheless, compared to observations, the diurnal variation in NO is predicted reasonably well. Similarly, calculated NO_2 concentrations are generally too low during the morning, and too large at night, although the simulated morning peak is consistent with measurements.

Statistical evaluation. The normalized gross error and normalized bias may be used to assess the model performance in simulating trace species distributions. The normalized gross error (E_{ng}) is defined as

$$E_{ng} = \frac{1}{N}\sum_{i=1}^{N}\frac{|p_i - o_i|}{o_i} \tag{8}$$

and the normalized bias (B_n) as

$$B_n = \frac{1}{N}\sum_{i=1}^{N}\frac{p_i - o_i}{o_i} \tag{9}$$

where N is the number of monitoring stations, and p_i and o_i are the predicted and observed concentrations at the ith station. These statistical measures are calculated each hour. In computing the statistics, the lower cutoff values on concentrations are 4 pphmv for ozone and 2 pphmv for NO, NO_2, CO, and NMHC. Tables 4 and 5 list some of the results for O_3, NO_2, and CO for the hours with the highest ozone concentrations. The average normalized gross errors (paired in space and time) in the SMOG ozone predictions are 29.2% and 25.8% on August 27 and 28, respectively. The corresponding normalized biases for ozone on these days are +3.1% and -2.3%, respectively. The technical guidance for photochemical modeling offered by the *California Air Resources Board (CARB)* [1992] suggests that a gross error of 35% and a bias of ±15% represent typical model performance for ozone prediction.

In the present simulations, the concentrations of nitrogen dioxide and carbon monoxide are typically lower than observations during daylight hours. Nitrogen dioxide is primarily a secondary pollutant generated from the oxidation of nitric oxide (although it is also emitted in small amounts). The concentrations of nitrogen dioxide are influenced by both the emissions of nitric oxide and NMHCs, as well as by the chemical mechanism. Carbon monoxide has relatively longer

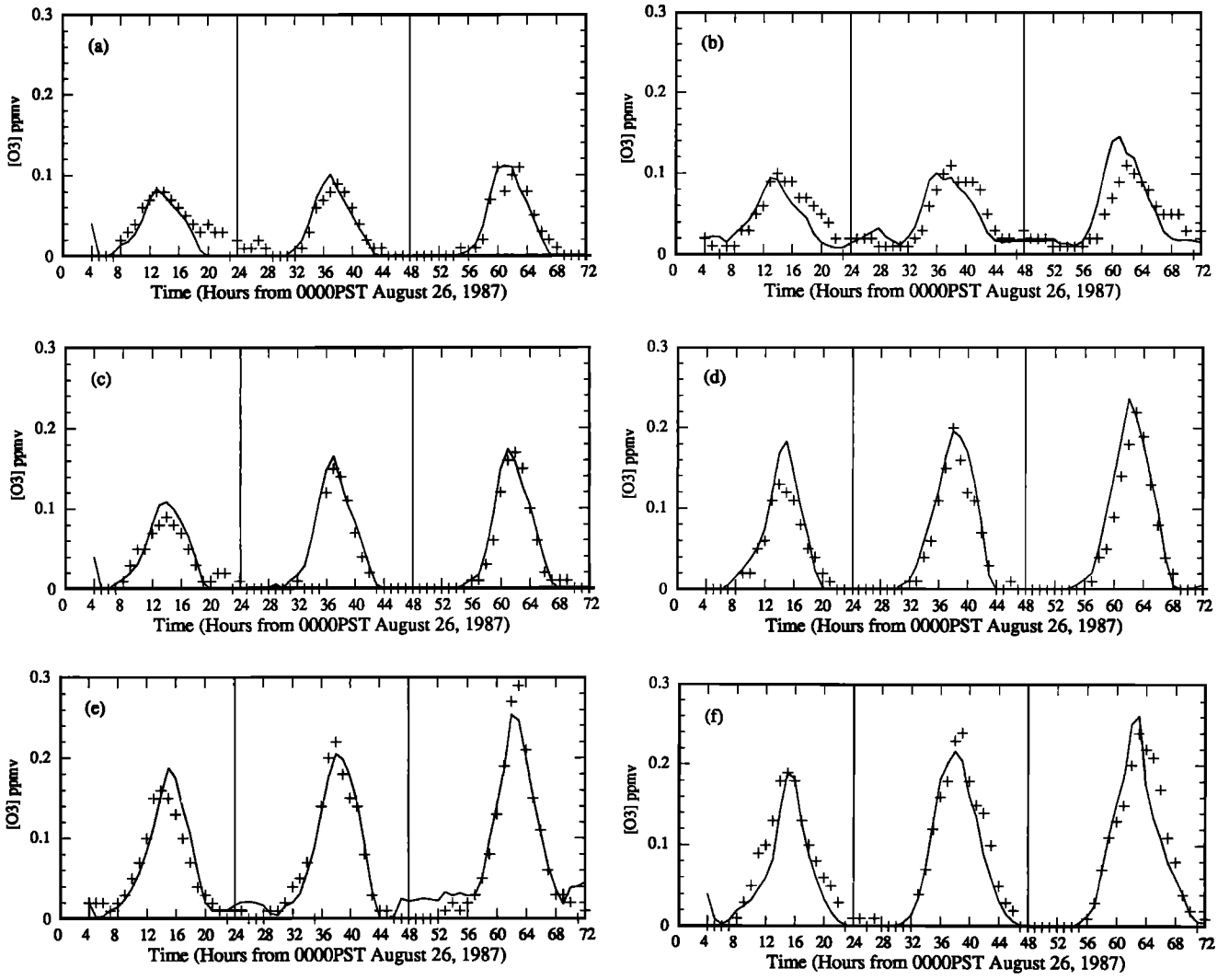

Figure 15. Time series of surface ozone concentrations (predicted, solid lines; observed, pluses) during the SCAQS observational period from August 26-28, 1987. The ozone variations are shown for (a) central Los Angeles (CELA), (b) El Toro (TORO), (c) Burbank (BURK), (d) Pomona (POMA), (e) Glendora (GLEN), and (f) Riverside-Rubidoux (RIVR). Refer to Figure 1 for locations of these monitoring sites.

lifetime, and its emissions and dispersion have the greatest effects on its distribution. During the day, the concentrations of nitric oxide at most stations were below the concentration cutoff value of 2 pphmv, and statistics were not calculated. Nonmethane hydrocarbon data were only available for three stations in the SCAQS data archive. In daylight hours, the SMOG model overestimated NO by only about 1%, and NMHCs by roughly 18%.

3.5. Sources of Uncertainty

The SMOG modeling system has a number of potential sources of error that may lead to discrepancies between predictions and observations. The uncertainties in input data and parameters, and approximations in the model physics, chemistry and numerical schemes, all contribute to the overall error in the predictions. Uncertainties in field measurements can also create inconsistencies. In the present analysis, differences between calculations and observations have four primary sources.

1. Errors in the input data, including initial and boundary conditions, land use information, and primary pollutant emission inventories, lead directly to discrepancies in the model results. Foremost among these problems is the recognition that emission inventories for key primary pollutants have large uncertainties at the present time. Estimates of emissions are based on empirical models, engineering analyses and limited test data rather than on systematic and detailed measurements at sources [*Fujita et al.*, 1992]. For example, the recent CARB inventory for the Los Angeles basin seriously underestimated mobile

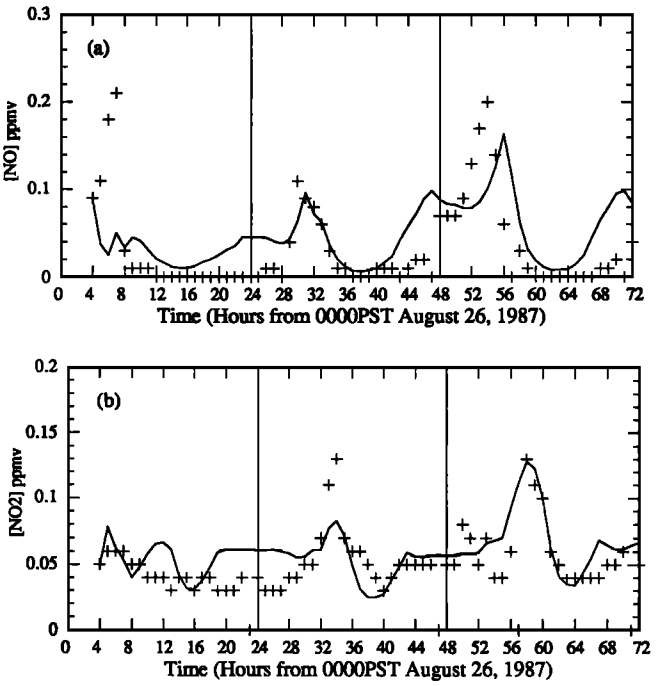

Figure 16. Time series of (a) NO and (b) NO_2 concentrations in the central Los Angeles (CELA) area during the SCAQS observational period from August 26-28, 1987. Predicted values are given by solid lines, and observed values are represented by pluses.

hydrocarbon emission sources, leading to significant errors in ozone predictions. Of secondary importance are uncertainties in the initial meteorological fields analyzed from a limited number of upper-air soundings, which may not be sufficient to represent fields over mountainous terrain. In addition, there are insufficient data available to initialize the concentrations of trace species properly over a large region. Uncertain meteorological and tracer boundary conditions can also produce errors that propagate into the model domain over time.

2. Approximations in the treatment of physical and chemical processes in the model can introduce additional errors and uncertainty in the results. For example, the effects of boundary layer turbulence are calculated using a hybrid boundary layer model rather than a high-order closure scheme. Clearly, the depth and evolution of the boundary layer are critical factors for accurate pollution forecasting. Organic chemistry is also crudely represented in models using lumped schemes such as the carbon-bond mechanism, involving surrogates and empirical reaction processes. While no complete treatment of organic photochemical kinetics is currently practical for regional modeling, the calibration of lumped mechanisms using smog chamber observations leaves considerable uncertainty unresolved. Assumptions in these, and other, representations of basic processes lead to differences between simulated and real atmospheres.

3. Numerical approximations employed to construct efficient algorithms for solving the complex set of equations describing air pollution can generate further errors. The computational solution for tracer advection, for example, is likely to induce artificial (numerical) diffusion and dispersion. The two-stream radiative transfer approximation provides an efficient approach for detailed calculations but introduces additional uncertainty into the radiation fields. Considering these issues, the present algorithms have been extensively tested and calibrated to insure that the errors lie within acceptable bounds.

4. Discretization of model solutions in space and time causes ambiguities related to finite resolution. The problem of resolution leads to obvious difficulties in comparing simulations and observations. Numerical models only resolve a small segment of the continuous spectra of spatial and temporal variations. For example, models yield grid-volume-averaged quantities that effectively define spatial variations only over scales greater than several grid lengths. Topography and other surface conditions, including chemical emissions, must typically be smoothed over the full area of a grid cell. The rates and effects of physical and chemical processes are calculated using grid-averaged quantities in nonlinear relationships. The ambiguities are particularly significant when gridded model predictions are compared to point measurements, in which small-scale influences are usually present.

In the present simulations, the model domain and grid spacing have been chosen as a compromise between predictive detail and computational efficiency. The algorithms used to solve the comprehensive treatment of physics and chemistry in the SMOG model have been extensively tested individually and by coupling them to other processes. Although potential errors might originate from various sources, the overall agreement between simulations and observations indicates that the model is well formulated and robust. Improvements to the present version of SMOG have already been integrated into the modeling system, including a

Table 4. Statistical Analysis of the O_3, NO_2 and CO Predictions for August 27, 1987

	O_3			NO_2			CO		
Time, PST	Stations	E_{ng}	B_n	Stations	E_{ng}	B_n	Stations	E_{ng}	B_n
1000	28	26.5	-8.2	22	41.0	-16.0	21	35.4	-22.2
1100	33	27.4	-5.3	22	40.2	-29.0	22	35.4	-29.4
1200	36	27.2	5.8	21	47.3	-47.3	22	34.2	-28.6
1300	36	26.4	7.9	21	54.8	-52.7	23	40.9	-39.9
1400	35	27.7	6.4	20	54.3	-53.8	21	44.7	-44.1
1500	37	25.1	2.5	20	54.8	-54.8	22	52.1	-52.1
1600	36	29.5	4.6	21	52.5	-49.3	22	49.2	-48.7
1700	34	33.8	6.2	20	43.9	-40.9	22	46.1	-44.0
1800	29	38.9	7.7	22	34.1	-25.5	21	35.7	-21.8
Average	33.8	29.2	3.1	21	47.0	-41.0	21.7	41.5	-36.8

Table 5. Statistical Analysis of the O_3, NO_2 and CO Predictions for August 28, 1987

	O_3			NO_2			CO		
Time, PST	Stations	E_{ng}	B_n	Stations	E_{ng}	B_n	Stations	E_{ng}	B_n
1000	23	25.0	-5.5	21	50.4	8.8	24	36.0	-0.6
1100	36	26.6	8.9	21	37.3	-6.4	24	38.9	-18.2
1200	36	21.1	5.1	22	35.5	-26.1	24	39.0	-30.6
1300	37	21.7	3.5	21	45.6	-43.6	23	37.9	-34.8
1400	37	22.7	-3.7	23	53.3	-53.3	21	43.8	-42.0
1500	37	24.6	-7.3	23	54.1	-54.1	22	42.8	-41.6
1600	36	27.6	-4.7	23	48.2	-44.6	22	45.3	-45.3
1700	34	27.7	-6.8	21	38.6	-28.0	22	41.5	-37.1
1800	33	35.0	-10.2	22	30.0	-10.6	23	38.7	-18.4
Average	34.3	25.8	-2.3	21.9	43.6	-28.7	22.7	40.4	-29.8

second-order turbulence parameterization, subgrid-scale cloud condensation processes, a detailed treatment of aerosol microphysics, and radiative transfer through clouds and aerosols. It is also important to reduce uncertainties in the emission data and other input parameters to improve the fidelity of air quality simulations in the Los Angeles basin.

4. Conclusions

The SMOG modeling system couples a meteorological dynamics/physics model, a tracer transport code, a chemistry and aerosol microphysics model, and a radiative transfer code to simulate air pollution in a complex airshed. The model has been applied to the Los Angeles basin for the conditions that existed on August 26-28, 1987, during the intensive SCAQS field program. The overall model performance was evaluated by comparing simulations against measurements collected by the SCAQS team.

The meteorological model exhibits considerable skill at predicting three-dimensional wind fields and boundary layer variations over complex topography in the southern California region. The main features of the surface flow patterns typically observed in the Los Angeles basin, such as convergence zones and flows across mountain passes, are clearly depicted in the simulations. Forecast variations in winds and temperatures near the surface, and in the structure and evolution of atmospheric boundary layer, are broadly consistent with observations in the Los Angeles basin. For surface parameters, the agreement index between predictions and measurements was in the range of 0.8-0.9 during daylight periods (1.0 would be perfect agreement). Vertical profiles of temperature and wind, likewise, exhibit general agreement between simulations and observations. Moreover, the movement and distributions of inert tracers released on August 28, 1987, are reproduced in considerable detail by the model, including the observed transfer of material through the Cajon Pass.

Predicted distributions and time variations of ozone and other chemically active pollutants have been compared with SCAQS observations on the days of interest. The standard emissions of reactive hydrocarbon precursors in the LA basin were adjusted upward using independent measurements of the ratio of nitrogen oxides to hydrocarbons. The spatial distributions of ozone calculated with the SMOG model are found to be in accord with a variety of measurements. Time series comparisons for surface ozone demonstrate that the SMOG simulations provide an excellent representation of the diurnal variation, peak concentration, and timing of maximum ozone abundances. The normalized gross errors for surface ozone concentrations during the daylight hours are 25 to 30% for the August 27-28 SCAQS episode. Remarkably, the SMOG simulations accurately predict the height, location, and evolution of the dense pollution layers detected over the basin. These oxidant layers have been shown in other work to contribute significantly to surface ozone concentrations [*Lu and Turco*, 1996].

The present analysis demonstrates the practicality of applying a comprehensive modeling system to study simultaneously and consistently regional meteorology and atmospheric chemistry. The SMOG model is designed to simulate coupled mesoscale and boundary layer dynamics, air pollution photochemistry, and aerosol microphysics and chemistry in a major urban airshed. The modeling system, with further improvements, should be applicable to a variety of air pollution problems in different urban settings worldwide.

Acknowledgments. This paper is based on Chapter 9 of Rong Lu's Ph.D. dissertation. The authors would like to thank Joseph Cassmassi and Satoru Mitsutomi of the Southern California Air Quality Management District (SCAQMD), and Bart Croes and Bruce Jackson at the California Air Resources Board, for providing SCAQS data. Computations were performed at the NASA Ames Research Center National Aeronautics Simulation facility (under project NAS-4802) and the EPA National Environmental Supercomputer Center. The work reported here was partially supported by the National Science Foundation under grant ATM-92-16646 and Environmental Protection Agency under grant CR 823755-01.

References

Allen, P. D. and K. K. Wagner, 1987 SCAQS emission inventory, magnetic tape numbers ARA806 and ARA807, Tech. Support Div., Calif. Air Resour. Board, Sacramento, 1992.

California Air Resources Board (CARB), Southern California air quality study (SCAQS) modeling data archive. Control strategy modeling section, Tech. Support Div., Sacramento, 1990.

CARB, Methodology to calculate emission factors for on-road motor vehicles, Tech. Support Div., Sacramento, 1991.

CARB, Technical guidance document: Photochemical modeling, Sacramento, 1992.

Chico, T., S. Mitsutomi, and J. C. Cassmassi, Assessing urban airshed model performance in the South Coast Air Basin using tracer gases, paper presented at the A&WMA Specialty Conference on Tropospheric Ozone and the Environment, A&WMA, Industry Hills, Calif., March 20-22, 1990.

England, W. G., and S. Marsh, SCAQS tracer study, in *Southern California Air Quality Study Data Analysis, Proceedings of an*

International Specialty Conference, July, 1992, Los Angeles, Calif., pp. 219-230, A&WMA, Pittsburgh, Penn., 1992.

Fujita, E. M., B. E. Croes, C. L. Bennett, D. R. Lawson, F. W. Lurmann, and H. H. Main, Comparison of emission inventory and ambient concentration ratios of CO, NMHC, and NO_x in California's South Coast Air Basin, *J. Air Waste Manage. Assoc., 42*, 264-276, 1992.

Harley, R. A., A. G. Russell, G. J. McRae, G. R. Cass, and J. H. Seinfeld, Photochemical modeling of the Southern California Air Quality Study, *Environ. Sci. Technol., 27*, 378-388, 1993.

Ingalls, M. N., L. R. Smith, and R. E. Kirksey, Measurement of on-road vehicle emission factors in the California South Coast Air Basin, Vol. I, Regulated emissions, Rep. *SwRI-1604*, Southwest Res. Inst. to the Coord. Res. Counc., Atlanta, Ga., 1989.

Jacobson, M. Z., Developing, coupling, and applying a gas, aerosol, transport, and radiation model to study urban and regional air pollution, Ph.D. thesis, Dep. of Atmos. Sci., Univ. of Calif., Los Angeles, 1994.

Jacobson, M. Z., and R. P. Turco, SMVGEAR: A sparse-matrix, vectorized Gear code for atmospheric models, *Atmos. Environ., 28A*, 273-284, 1994.

Jacobson, M. Z., and R. P. Turco, Simulating condensational growth, evaporation, and coagulation of aerosols using a combined moving and stationary size grid, *Aerosol Sci. Technol., 22*, 73-92, 1995.

Jacobson, M. Z., and P. R. Turco, E. J. Jensen, and O. B. Toon, Modeling coagulation among particles of different composition and size, *Atmos. Environ., 28A*, 1327-1338, 1994.

Jacobson, M. Z., R. Lu, P. R. Turco, and O. B. Toon, Development and application of a new air pollution model system, I, Gas-phase simulations, *Atmos. Environ., 30B*, 1939-1963, 1996a.

Jacobson, M. Z., A. Tabazadeh, and R. P. Turco, Simulating equilibrium within aerosols and nonequilibrium between gases and aerosols, *J. Geophys. Res., 101*, 9079-9091, 1996b.

Keyser, D., and R. A. Anthes, The applicability of a mixed-layer model of the planetary layer to real-data forecasting., *Mon. Weather Rev., 105*, 1351-1370, 1977.

Lawson, D. R., The southern California air quality study, *J. Air Waste Manage. Assoc., 40*, 156-165, 1990.

Lu, R., Development of an integrated air pollution modeling system and simulations of ozone distributions over the Los Angeles basin, Ph.D. dissertation, Univ. of Calif., Los Angeles, 1994.

Lu, R., and R. P. Turco, Air pollution transport in a coastal environment, I, Two-dimensional simulation of sea-breeze and mountain effects, *J. Atmos. Sci., 51*, 2285-2308, 1994.

Lu, R., and R. P. Turco, Air pollution transport in a coastal environment, II, Three-dimensional simulations over the Los Angeles basin, *Atmos. Environ., 29B*, 1499-1518, 1995.

Lu, R., and R. P. Turco, Modeling of three-dimensional ozone distributions over the Los Angeles basin, *Atmos. Environ., 30*, 4155-4176, 1996.

Lu, R., R. P. Turco, and M. Z. Jacobson, An integrated air pollution modeling system for urban and regional scales, 1, Structure and performance, *J. Geophys. Res.*, this issue.

Pielke, R. A., *Mesoscale meteorological modeling*, 612 pp., Academic, New York, 1984.

Pierson, W. R., N. F. Robinson, and A. W. Gertler, Review and reconciliation of on-road emission factors in the SoCAB, in *Southern California Air Quality Study Data Analysis, Proceedings of an International Specialty Conference, July, 1992, Los Angeles, Calif.*, pp. 35-42, A&WMA, Pittsburgh, Penn., 1992.

Roberts, P., and H. Main, Analysis of 3-D air quality data and carbon, nitrogen, and sulfur species distributions during the Southern California Air Quality Study, final report, CRC contract SCAQS-8-4, Coord. Res. Counc., Atlanta, Ga., 1992.

Southern California Air Quality Management District (SCAQMD), *Draft AQMP 1991 Revision Technical Report V-B Ozone Modeling - Performance Evaluation*, Diamond Bar, Calif., December, 1990.

SCAQMD, *Final AQMP 1991 Revision Technical Report V-B Ozone Modeling - Performance Evaluation*, Diamond Bar, Calif., July, 1991.

Tesche, T. W., P. Georgopoulos, J. H. Seinfeld, G. Cass, F. L. Lurmann, and P. M. Roth, Improvement of procedures for evaluating photochemical models, Report to the California Air Resources Board, contract A832-103, Radian Corp., Sacramento, Calif., 1990.

Ulrickson, B. L., and C. F. Mass, Numerical investigation of mesoscale circulations over the Los Angeles basin, II, Synoptic influences and pollutant transport. *Mon. Weather Rev., 118*, 2162-2184, 1990.

Willmott, C. J., On the validation of models, *Phys. Geog., 2*, 184-194, 1981.

Willmott, C. J., S. G. Ackleson, R. E. Davis, J. J. Feddema, K. M. Klink, D. R. Legates, J. O'Donnell, and C. M. Rowe, Statistics for the evaluation and comparison of models, *J. Geophys. Res., 90*, 8995-9005, 1985.

M. Z. Jacobson, Department of Civil Engineering, Stanford University, Stanford, CA 94305-4020. (e-mail: jacobson@ce.stanford.edu)

R. Lu and R. P. Turco, Department of Atmospheric Sciences, University of California, 405 Hilgard Avenue, Los Angeles, CA 90095-1565. (e-mail: rongl@atmos.ucla.edu; turco@atmos.ucla.edu)

(Received September 6, 1995; revised October 28, 1996; accepted October 28, 1996.)